RSC Applied Interfaces

ROYAL SOCIETY OF CHEMISTRY

PAPER

View Article Online
View Journal

Cite this: DOI: 10.1039/d5lf00408j

Bifunctional Pd sites on Pd_4/Co_3O_4 nanowires for high selectivity of pyrazine electrocatalytic hydrogenation with water as the hydrogen source

Fangcheng Qiu,[a] Siyi Chen,[b] Xin Zheng,[a] Hanyu Li,[a] Bowen Chen,[b] Shaowen Tan,[b] Xue Han[b] and Shengping Wang *[b]

Received 28th December 2025,
Accepted 17th February 2026

DOI: 10.1039/d5lf00408j

rsc.li/RSCApplInter

Liquid organic hydrogen carriers (LOHCs) are considered highly promising materials for hydrogen storage. However, hydrogenation and dehydrogenation of LOHCs often require harsh reaction conditions. The hydrogenation of nitrogen-containing heterocyclic organic molecules in aqueous media is particularly challenging. This work presents an efficient electrochemical hydrogen storage system based on pyrazine as a nitrogen-containing organic hydrogen carrier. In this electrochemical system, water serves as both the solvent and the hydrogen source for pyrazine hydrogenation. Pd_4/Co_3O_4/NF demonstrates high electrochemical activity under ambient temperature and pressure. At −0.25 V (*vs.* RHE), the hydrogenation conversion rate of pyrazine reaches 99.4% with the selectivity rate of 97.1%. Pd acts as the catalytic active center. It not only promotes water electrolysis to generate H* but also facilitates the adsorption of pyrazine, providing sites for its hydrogenation. Pd_4/Co_3O_4/NF maintains high catalytic activity after 8 cycles, showing excellent stability. This electrochemical hydrogenation of pyrazine proceeds without using hydrogen gas. Therefore, the system offers superior safety performance.

1 Introduction

The rapid depletion of fossil fuels and severe environmental pollution have made the development of new energy sources a major global focus.[1] Hydrogen, as a clean energy carrier, is regarded as an ideal alternative to address the world's energy and environmental challenges.[2] However, its large-scale application is hindered by the challenge of developing efficient, safe, and economical storage and transportation methods.[3] Currently, compressed hydrogen storage is widely used due to its low cost and simple operation.[4] Yet, it suffers from low volumetric density and safety concerns. Liquid hydrogen storage offers higher density, suitable for large-scale, long-distance transport.[5] However, it requires expensive cryogenic equipment and faces evaporation loss risks. Solid-state hydrogen storage materials, like carbon-based materials, metal hydrides, and MOFs, provide better safety.[6] However, they often require harsh conditions for hydrogenation/dehydrogenation and show poor reversibility. Recently, liquid organic hydrogen carriers (LOHCs) have shown great promise for large-scale hydrogen logistics.[7] They offer good reversibility, high hydrogen capacity, and compatibility with existing fuel infrastructure. Aromatic hydrocarbons of LOHCs have been widely studied with capacities of 6.1–7.3 wt%, but their catalytic hydrogenation and dehydrogenation typically need high temperatures (200–400 °C). The research indicates that nitrogen-containing heterocyclic compounds (N-LOHCs) can significantly lower the energy demands of these processes.[8] Examples like *N*-propylcarbazole, 1-methylindole, *N*-ethylindole, and 7-ethylindole demonstrate excellent performance.[9–13] The thermal catalytic hydrogenation/dehydrogenation for N-LOHCs still requires temperatures of 120–200 °C. It often relies on flammable hydrogen gas or other expensive, toxic hydrogen sources, posing safety and environmental risks.

Electrocatalytic technology holds broad applications in the hydrogen energy sector. Compared to thermal catalysis, it offers advantages such as milder reaction conditions, easily tunable selectivity, and the direct use of water as a hydrogen source.[14] Pan *et al.* employed water as the hydrogen source and achieved complete conversion of 10 mM quinoline with nearly 100% selectivity over a non-precious Cu-based catalyst after 1 h at a potential of −1.275 V (*vs.* Hg/HgO). Their work revealed that Cu^+–Cu^0 dual sites promote hydrogenation *via* a proton-coupled electron transfer (PCET) mechanism, and the coupled system (ECH||BAOR) operates at a lower voltage with higher efficiency.[15] Guo *et al.* reported a fluorine-modified cobalt (Co–F) catalyst that enables high-yield hydrogenation of quinoline at room temperature. Under an optimal

[a] *Electric Power Research Institute, Yunnan Power Grid Co., Ltd, Kunming 650220, China*
[b] *Faculty of Material Science and Chemistry, China University of Geosciences, Wuhan 430074, China. E-mail: spwang@cug.edu.cn*

potential of −1.1 V (*vs.* Hg/HgO), 0.1 mmol quinoline was fully converted within 6 h with 99% selectivity.[16] A $MoNi_4$ catalyst achieved 99% yield of tetrahydroquinoxaline from 0.3 mM quinoxaline within 1 h through consecutive PCET steps at a very low overpotential of −0.05 V (*vs.* RHE).[17] Such electrochemical hydrogen storage systems are safer, more environmentally friendly, and simpler to operate, demonstrating promising application prospects. Existing research has predominantly focused on quinoline and quinoxaline. In these compounds, hydrogenation and dehydrogenation occur only in the N-heterocyclic part of the bicyclic structure, resulting in a relatively low gravimetric hydrogen storage capacity. Moreover, both compounds exhibit poor solubility, making them less ideal as substrates for electrocatalytic LOHC-based hydrogen storage. Recent studies have used Rh/KB as a cathode catalyst in an anion-exchange membrane (AEM) electrolyzer to reduce nitrogen-containing aromatic compounds and for the first time accomplished the electrocatalytic hydrogenation of pyrazine with a yield of 96%.[18] Pyrazine offers a considerable theoretical hydrogen storage capacity of 6.97% and is fully miscible with water, rendering it a more promising candidate for hydrogen storage carriers.

The efficiency of LOHC electrochemical hydrogenation (ECH) is primarily determined by the availability of H*. Therefore, developing electrocatalysts with excellent water dissociation capability and modulating the adsorption/desorption behavior of organic molecules on the electrode surface are key to achieving highly efficient LOHC conversion. Noble metals such as Pd, Pt, Ru, and Ir are widely studied due to their optimal H* adsorption/desorption properties.[19,20] Pd exhibits strong H* adsorption capability, second only to Pt among them. Additionally, its cost is significantly lower. Under ambient conditions, H^+ ions can occupy the octahedral sites in the Pd lattice, leading to the formation of PdH_n.[21] Pd shows high adsorption selectivity, fast kinetics, and good reversibility, making it highly promising for ECH. It demonstrates the highest catalytic activity for the hydrogenation of aromatic aldehydes.[22] The weak adhesion between the active Pd phase and the substrate typically results in a low loading mass, which limits the number of available active sites.[23] Furthermore, Pd nanoparticles are prone to detach from the substrate during prolonged operation or at high current densities. Thus, strong interfacial contact is crucial for electron conductivity and catalytic stability. Co_3O_4 can anchor and disperse catalyst nanoparticles as a substrate material. This enhances the loading of active components and provides abundant catalytic sites.[24] The strategies involving defect engineering, doping, and constructing heterointerfaces have emerged as promising approaches to tune the electronic structure of Co_3O_4 and improve its overall catalytic performance.[25] For instance, the strong electronic coupling at the interface between RuO_2 and Co_3O_4 accelerates reaction kinetics and enhances catalyst stability. The heterointerface in RuO_2@Co_3O_4 not only directly participates in the reaction but also modulates the d-band center of the catalyst. This optimization adjusts the adsorption strength of key intermediates, thereby improving the hydrogen evolution reaction (HER) activity.[26] Liao *et al.* confirmed the presence of a strong metal–support interaction between Au nanoparticles and oxygen vacancy-rich Co_3O_4 nanorods (Co_3O_4 NRs–OVs). This interaction facilitates electron transfer from Co_3O_4 NRs–OVs to Au. The increased electron density on the Au surface selectively adsorbs the C═O group of vanillin and promotes catalytic hydrogen transfer for alcohol production.[27] Similarly, an Ir–Co_3O_4 electrocatalyst with low Ir content and abundant oxygen vacancies (O_V) has been developed. This catalyst features rich three-dimensional active sites, rapid electron transfer, and oxygen-vacancy-induced optimized kinetics for oxygenated intermediate formation. These properties collectively enhance the oxygen evolution reaction (OER) performance in acidic environments.[28]

In this work, a series of Pd_x/Co_3O_4/NF as ECH electrocatalysts of pyrazine with heterointerfaces and high O_V content were synthesized *via* a room-temperature reduction method. The Co_3O_4 layer was directly grown on the nickel foam (NF) surface. This approach not only provided abundant anchoring sites for Pd loading but also created a tight interfacial structure. It avoided issues associated with polymer binders, thereby effectively improving the utilization of active components. Cobalt atoms modulated the electronic structure of the catalysts. Through strong metal–support interaction, they regulated the adsorption and activation of reaction substrates. This enhancement strengthened the adsorption–desorption behavior of Pd towards H* atoms and organic molecules. Pyrazine was selected as the hydrogen carrier; the pyrazine hydrogenation to produce piperazine had a theoretical hydrogen storage density of 6.97 wt%. The effects of Pd loading, catalyst morphology, and electrochemical performance on the ECH behavior of pyrazine were systematically investigated, and the hydrogenation mechanism was also studied. Pd_4/Co_3O_4/NF exhibited high electrocatalytic activity for the hydrogenation of pyrazine and dehydrogenation of piperazine. It achieved optimal hydrogenation conversion and selectivity. The hydrogenation mechanism revealed that the water-mediated ECH process completely eliminates safety risks associated with the use of external hydrogen gas. In summary, this electrochemical hydrogen storage system is mild, rapid, efficient, and simple. It overcomes the practical limitations of traditional methods.

2 Experimental

2.1 Catalyst preparation

Preparation of Pd_x/Co_3O_4/NF. NF (2 cm × 3 cm × 3 mm) was sequentially ultrasonically cleaned in absolute ethanol, 2 M hydrochloric acid, and absolute ethanol again, for 5 min each. Afterwards, it was rinsed thoroughly and air-dried. The homogeneous solution prepared by dissolving 1.746 g of $Co(NO_3)_2{\cdot}6H_2O$ (0.03 M), 0.617 g of NH_4F (0.083 M), and 1.401 g of urea (0.05 M) in 50 mL of deionized water, along with the pretreated NF, was transferred into a 100 mL Teflon-

lined autoclave. The autoclave was subjected to a hydrothermal reaction at 120 °C for 6 h. The resulting precursor was collected and sequentially washed with absolute ethanol and deionized water. It was then dried in a vacuum oven at 60 °C for 8 h. Finally, the precursor was calcined in a muffle furnace at 400 °C for 3 h under an air atmosphere to obtain Co_3O_4/NF.

Different amounts of $PdCl_2$ (1.2 mM, 1.8 mM, 2.4 mM, 3.0 mM) and corresponding amounts of NaCl (2.4 mM, 3.6 mM, 4.8 mM, 6.0 mM) were added to separate 50 mL portions of deionized water. These mixtures were magnetically stirred in a constant-temperature water bath at 40 °C for 30 min until they turned clear and orange-yellow. The Co_3O_4/NF precursor was fixed and fully immersed in each clear solution. Stirring was continued at 40 °C until the solution color changed from orange-yellow to colorless and transparent. The catalyst was then retrieved, rinsed with deionized water, and dried overnight at room temperature. The resulting catalysts were designated as Pd_2/Co_3O_4/NF, Pd_3/Co_3O_4/NF, Pd_4/Co_3O_4/NF, and Pd_5/Co_3O_4/NF.

2.2 Material characterization

The morphology and elemental distribution of the samples were determined *via* a Hitachi SU8010 scanning electrode microscope (SEM) equipped with an X-ray energy dispersive spectrometer (EDS). The crystallinity of the electrocatalysts was characterized by X-ray diffraction (XRD) using a Bruker/D8 advance powder diffractometer with Cu Kα radiation (λ = 1.5418 Å) with a scanning range of 5° to 90° and a scan rate of 10° min^{-1}. X-ray photoelectron spectroscopy (XPS) was carried out using a Thermo Fisher ESCALAB 250Xi X-ray photoelectron spectrometer with Al Kα X-ray radiation. The binding energy of C 1s = 284.80 eV was used as the energy standard for charge correction.

The concentrations of pyrazine/piperazine in the electrolyte were quantified using gas chromatography (GC, Panno A60). The GC system was equipped with an AB-1 column (30 m × 0.32 mm × 0.25 μm). The injector temperature, detector temperature, and oven temperature were all set at 300 °C. The oven temperature program involved ramping from 70 °C to 180 °C at a rate of 10 °C min^{-1}.

To ensure analytical reliability, a strict standardization protocol was followed. High-purity commercial standards of pyrazine and piperazine were used to identify their GC retention times. The standard solutions (0.1–1.0 mg mL^{-1}) were analyzed in quintuplicate to establish a linear calibration curve relating peak area to concentration. All catalytic samples were quantified using this external standard method to calculate pyrazine conversion and piperazine selectivity (Fig. S1).

2.3 Electrochemical measurements

2.3.1 Electrochemical system. All procedures, including electrolyte preparation, cell assembly, and electrochemical testing, were performed inside an argon-filled glove box (at ~1 atm) at 25 °C. The prepared electrolyte was purged with argon for 1 h to remove dissolved gases. The electrochemical tests were conducted using a CHI660D electrochemical workstation within an H-type electrochemical cell equipped with a glass frit.

A catalyst electrode (10 mm × 10 mm) served as the working electrode. A platinum electrode (10 mm × 10 mm) and an Hg/HgO electrode were used as the counter electrode and reference electrode, respectively. The Hg/HgO electrode was filled with 1 M KOH as the internal electrolyte without a salt bridge. The electrolyte in the working electrode compartment was 40 mL of 1 M KOH containing 10 mM pyrazine (or just 40 mL of 1 M KOH for control experiments), with a magnetic stirring rate of 400 rpm. The counter electrode compartment contained 40 mL of 1 M KOH (pH = 13.8).

All measured potentials were converted to the reversible hydrogen electrode (RHE) scale using the Nernst equation (eqn (1)).

$$E_{RHE}\,(V) = E_{(Hg/HgO)} + 0.059 \times pH + E^{0}_{(Hg/HgO)} = E_{(Hg/HgO)} + 0.059 \times pH + 0.098 \quad (1)$$

2.3.2 Linear sweep voltammetry and cyclic voltammetry. The synthesized electrocatalysts were used as working electrodes for linear sweep voltammetry (LSV) and cyclic voltammetry (CV) tests. The potential window for both LSV and CV measurements was set from 0.7 V to −0.45 V (*vs.* RHE) with a scan rate of 5 mV s^{-1}, and the scan direction was from 0.7 V to −0.45 V (*vs.* RHE).

2.3.3 Tafel. The Tafel slopes were calculated *via* linear fitting of selected data regions from the LSV results. This was done to evaluate the kinetic reaction rates of the catalysts. The Tafel slope was determined using eqn (2).

$$\eta = a + b \times \log j \quad (2)$$

where η (V) represents the overpotential, j (mA cm^{-2}) is the current density, b (mV dec^{-1}) is the Tafel slope, and a (V) is the Tafel constant, representing the overpotential corresponding to a unit current density (1 mA cm^{-2}).

2.3.4 Electrochemical impedance spectroscopy. Electrochemical impedance spectroscopy (EIS) measurements were conducted at −0.25 V (*vs.* RHE) with a frequency range of 10^5 Hz to 10^{-2} Hz and an amplitude of 5 mV. The data were fitted using Zview software and an equivalent circuit model to determine the electrochemical parameters.

2.3.5 Electrochemical active surface area. CV tests were performed at 20, 40, 60, 80, and 100 mV s^{-1} to determine the double-layer capacitance (C_{dl}). The potential range was set from open circuit potential (OCP) −50 mV to OCP +50 mV. The electrochemical active surface area (ECSA) was then calculated using eqn (3).

$$ECSA = C_{dl}/C_s \quad (3)$$

where C_s is the specific capacitance, taken as 0.04 mF cm^{-2} in this study.[29]

2.3.6 Chronoamperometry. The hydrogenation reaction of pyrazine was conducted at a constant potential of −0.2 V (*vs.* RHE) for 2 h. The contents of pyrazine and piperazine in the electrolyte were measured by GC. The conversion rate of pyrazine and the selectivity for piperazine were then calculated using eqn (4) and (5).

$$\text{Conversion rate}\ (\%) = \frac{M_1}{M_2} \times 100\% \quad (4)$$

$$\text{Selectivity rate}\ (\%) = \frac{M_3}{M_1} \times 100\% \quad (5)$$

where M_1 (mol) represents the amount of substrate consumed, M_2 (mol) represents the amount of initial substrate, and M_3 (mol) represents the amount of target product formed.

3 Results and discussion

3.1 Material characterization

3.1.1 XRD and XPS. The XRD diffraction peaks at 19.06°, 31.28°, 36.85°, 38.61°, 44.65°, 55.58°, 59.33°, 65.16°, and 76.55° of Co_3O_4/NF correspond to the (111), (220), (311), (222), (400), (422), (511), (440), and (533) crystal planes of Co_3O_4 (PDF#78-1970) respectively (Fig. 1a),[30] and those at 44.65°, 51.95°, and 76.55° were attributed to NF (PDF#87-0712).[31] The peaks of Pd_4/Co_3O_4/NF were observed at 19.07°, 31.36°, 36.91°, 38.63°, 44.66°, 55.68°, 59.35°, 65.23°, and 76.60°, which matched the (111), (220), (311), (222), (400), (422), (511), (440), and (533) planes of Co_3O_4 (PDF#78-2177), respectively,[30] and those at 44.66°, 51.97°, and 76.57° again originated from NF (PDF#87-0712). Additionally, the peaks at 40.28°, 82.34° belong to the (111) and (311) planes of metallic Pd (PDF#88-2335).[32] Pd was primarily present in the metallic Pd^0 state on the Co_3O_4/NF surface, indicating the successful preparation of the catalyst. Notably, compared to the diffraction peaks of Co_3O_4 (PDF#78-2177) in Co_3O_4/NF, those in Pd_4/Co_3O_4/NF showed a slight positive shift. This shift was attributed to lattice contraction or distortion induced by the presence of O_Vs. This lattice distortion induced micro strain within the material and resulted in high surface energy, enhancing the metal–support interaction.[27]

The Co 2p XPS spectrum of Co_3O_4/NF showed two main peaks at 779.79 and 795.04 eV, which were attributed to Co $2p_{3/2}$ and Co $2p_{1/2}$, respectively (Fig. 1b). Specifically, the

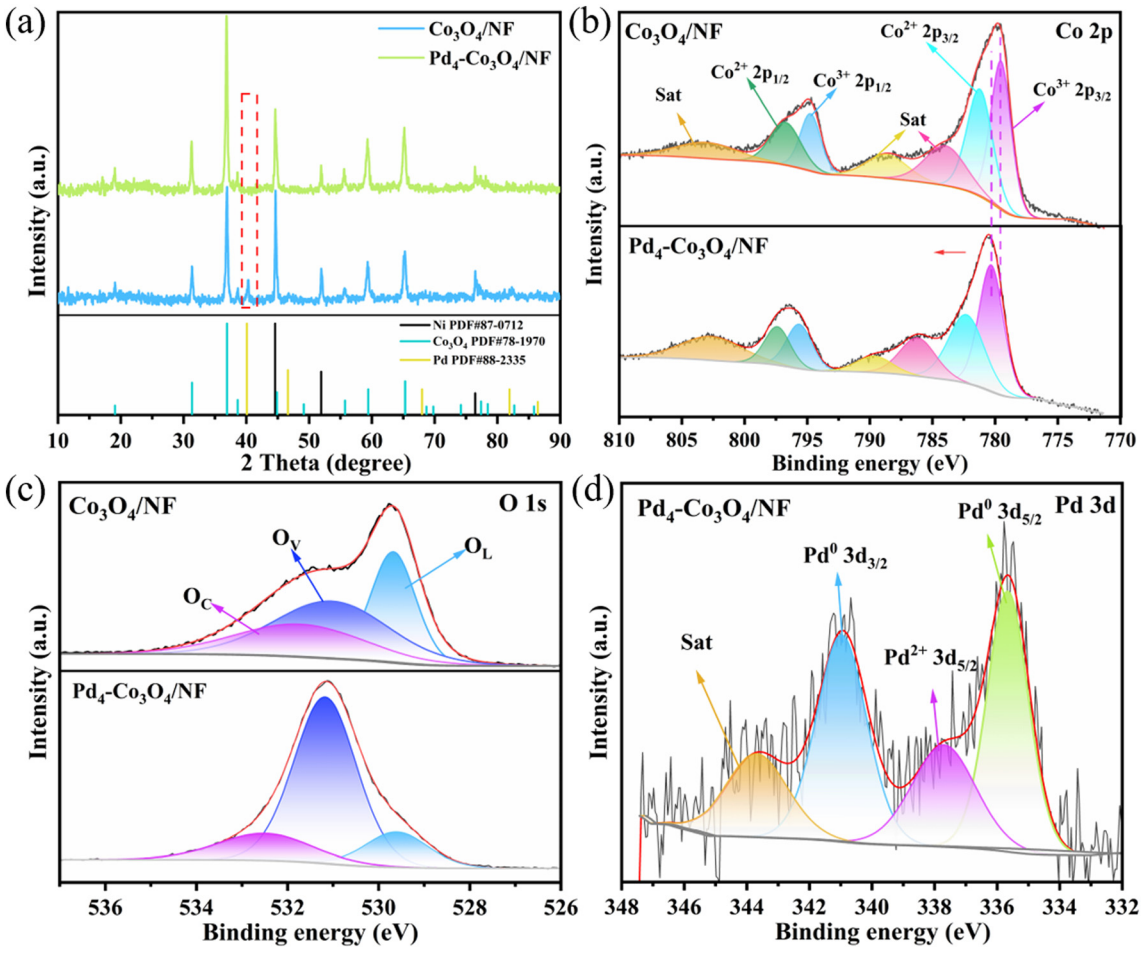

Fig. 1 (a) XRD patterns and (b) Co 2p, (c) O 1s, (d) Pd 3d XPS spectra of Co_3O_4/NF and Pd_4/Co_3O_4/NF.

peaks at 779.49 and 794.68 eV were assigned to Co^{3+}, and those at 781.18 and 796.68 eV were assigned to Co^{2+}.[33] The peak intensity of Co^{3+} was significantly higher than that of Co^{2+}, which was consistent with the XRD results. For the Pd 3d spectrum of Pd_4/Co_3O_4/NF, the peak at 343.67 eV was identified as a satellite peak, and those at 335.67 and 340.94 eV were assigned to Pd^0 $3d_{5/2}$ and Pd Pd^0 $3d_{3/2}$, respectively (Fig. 1d). A peak corresponding to Pd^{2+} $3d_{5/2}$ was observed at 337.72 eV.[34] In the Co 2p spectrum, the peaks at 780.54 and 796.45 eV belonged to Co $2p_{3/2}$ and Co $2p_{1/2}$, respectively (Fig. 1b). The separation of these peaks by a spin–orbit splitting confirmed the coexistence of Co^{3+} and Co^{2+}.[35] The peaks at 780.32 and 795.00 eV were attributed to Co^{3+}, and those at 782.29 and 797.34 eV were attributed to Co^{2+}. Additionally, the peaks at 786.29, 789.66 and 802.78 eV were identified as satellite peaks associated with Co $2p_{3/2}$ and Co $2p_{1/2}$, characteristic of the spinel structure.[35]

Compared with the Co $2p_{3/2}$ binding energy of Co_3O_4/NF, that of Pd_4/Co_3O_4/NF increased. This suggested spontaneous electron transfer from cobalt (electronegativity of 1.88) to the more electronegative palladium (electronegativity of 2.20), rendering the Pd species more electron-rich.[34] The increased electron filling caused a downshift in the d-band center of Pd. According to the d-band center theory, this downshift typically led to a moderate weakening of adsorption energy. This optimized adsorption strength contributed to higher activity and selectivity. The results further confirmed that Pd primarily existed in the metallic Pd^0 state. The presence of Pd^{2+} indicated a strong interaction between the Pd nanoparticles and the substrate. This interaction was beneficial for enhancing the long-term stability of Pd_4/Co_3O_4/NF during the ECH process (Fig. 1d).

Both Co_3O_4/NF and Pd_4/Co_3O_4/NF exhibited three oxygen states. O_L was attributed to typical metal–oxygen bonds, O_V was associated with oxygen vacancies related to defects with low oxygen coordination and O_C resulted from the physical and chemical adsorption of water on the material's surface.[36] In the O 1s spectrum of Pd_4/Co_3O_4/NF, the peaks at 529.55, 531.13, and 532.45 eV corresponded to O_L, O_V and O_C, respectively (Fig. 1c). Compared to Co_3O_4/NF, the O_V concentration in Pd_4/Co_3O_4/NF was significantly higher. These positively charged defect centers indirectly influenced the adsorption capacity of Pd metal sites by altering the local electron density. The O_V increase promoted catalysis and enhanced the intrinsic catalytic activity.[28]

3.1.2 SEM and EDS. The SEM images show that Co_3O_4/NF exhibited a tightly packed nanoneedle structure (Fig. 2a–c). This inherent structure provided a much higher specific surface area compared to conventional particles or sheets, offering an extensive platform for Pd loading. After Pd deposition, the SEM images of Pd_2/Co_3O_4/NF, Pd_3/Co_3O_4/NF, Pd_4/Co_3O_4/NF, and Pd_5/Co_3O_4/NF showed that Pd was loaded onto the Co_3O_4/NF surface as irregular clusters. The structures of Pd_2/Co_3O_4/NF, Pd_3/Co_3O_4/NF, and Pd_4/Co_3O_4/NF were similar, with numerous fine particles forming a covering layer on the tips of the Co_3O_4 nanoneedles (Fig. 2d–l).

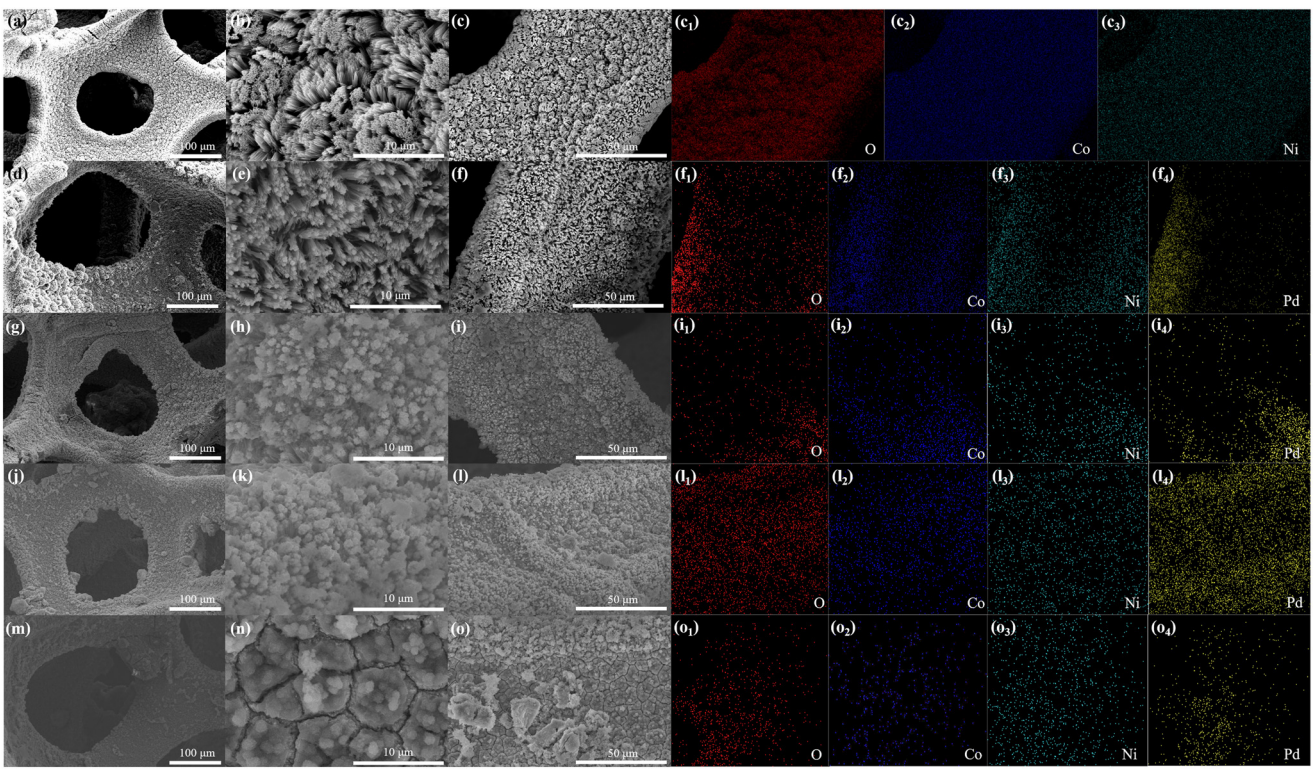

Fig. 2 SEM images of (a–c) Co_3O_4/NF, (d–f) Pd_2/Co_3O_4/NF, (g–i) Pd_3/Co_3O_4/NF, (j–l) Pd_4/Co_3O_4/NF, and (m–o) Pd_5/Co_3O_4/NF, and the corresponding EDS mappings of (c_{1-3}) Co_3O_4/NF, (f_{1-4}) Pd_2/Co_3O_4/NF, (i_{1-4}) Pd_3/Co_3O_4/NF, (l_{1-4}) Pd_4/Co_3O_4/NF, and (o_{1-4}) Pd_5/Co_3O_4/NF.

However, the particle size increased with higher Pd loading. Pd_4/Co_3O_4/NF achieved the optimal balance between dispersion and loading amount. It provided the highest number of exposed active sites without severely clogging the pores between the nanowires. This sample featured more numerous and densely packed Pd clusters (Fig. 2j–l). This increased the coverage of the active metal, enhanced the electrochemically active surface area and provided ample opportunities for contact between pyrazine and the active sites. A further increase in Pd loading (Pd_5/Co_3O_4/NF) disrupted the needle-like structure of Co_3O_4/NF, significantly reducing the active surface area (Fig. 2m–o). The EDS mapping confirmed the uniform distribution of all elements in the catalysts.

3.2 Electrochemical tests

3.2.1 CV. There were no distinct redox peaks of the CV curves for NF and Co_3O_4/NF within the potential range of −0.45 V to 0.7 V (*vs.* RHE) in both electrolytes (1 M KOH and 1 M KOH + 0.01 M pyrazine) (Fig. 3a and b). Furthermore, both NF and Co_3O_4/NF exhibited weak HER activity.[37] In 1 M KOH + 0.01 M pyrazine, the CV curves for Pd_2/Co_3O_4/NF, Pd_3/Co_3O_4/NF, Pd_4/Co_3O_4/NF and Pd_5/Co_3O_4/NF showed a broad redox peak. The peak current increased with higher Pd loading. An oxidation peak appeared at ~0.25 V (*vs.* RHE) suggesting it corresponds to the oxidation of Pd (Fig. 3c–f).[38] The differences between the CV profiles of these Pd-containing catalysts and that of Co_3O_4/NF also confirmed the successful incorporation of Pd and the resultant structural modification.

3.2.2 LSV. NF in 1 M KOH at −0.25 V (*vs.* RHE) exhibited a HER current of −20.7 mA cm^{-2}, indicating its limited ability to supply H* (Fig. 4a and Table S1). In 1 M KOH + 0.01 M pyrazine, the current density of NF at −0.25 V (*vs.* RHE) increased to −29.1 mA cm^{-2}. This net current increase suggested that NF has some affinity for adsorbing pyrazine.[31] The LSV curves of Co_3O_4/NF showed little difference between the two electrolytes, and its HER current in 1 M KOH at −0.25 V (*vs.* RHE) was −23.9 mA cm^{-2}, only slightly higher than that of NF (Fig. 4a). This indicated that the Co species alone had minimal adsorption or catalytic effect on pyrazine. Compared to the current density of NF in 1 M KOH, those of Pd_x/Co_3O_4/NF increased significantly. This demonstrated that Pd promoted the HER, thereby facilitating H* generation. The HER currents for Pd_2/Co_3O_4/NF, Pd_3/Co_3O_4/NF, Pd_4/Co_3O_4/NF, and Pd_5/Co_3O_4/NF at −0.25 V (*vs.* RHE) were −30.5, −38.0, −40.3, and −39.0 mA cm^{-2}, respectively. In 1 M KOH + 0.01 M pyrazine, the current densities at the same potential became −39.4, −45.2, −77.8, and −40.8 mA cm^{-2}, respectively. Pd_4/Co_3O_4/NF showed the highest HER current and the largest net current. A more negative potential resulted in a larger net current, indicating stronger adsorption and catalytic activity towards the pyrazine molecule (Fig. 4a).[16] It was reasonably inferred that the Pd sites acted as active centers for both H* generation and pyrazine adsorption.[39] The extended d-orbitals of Pd enabled stronger interaction with the π-system of pyrazine, facilitating strong adsorption. Compared

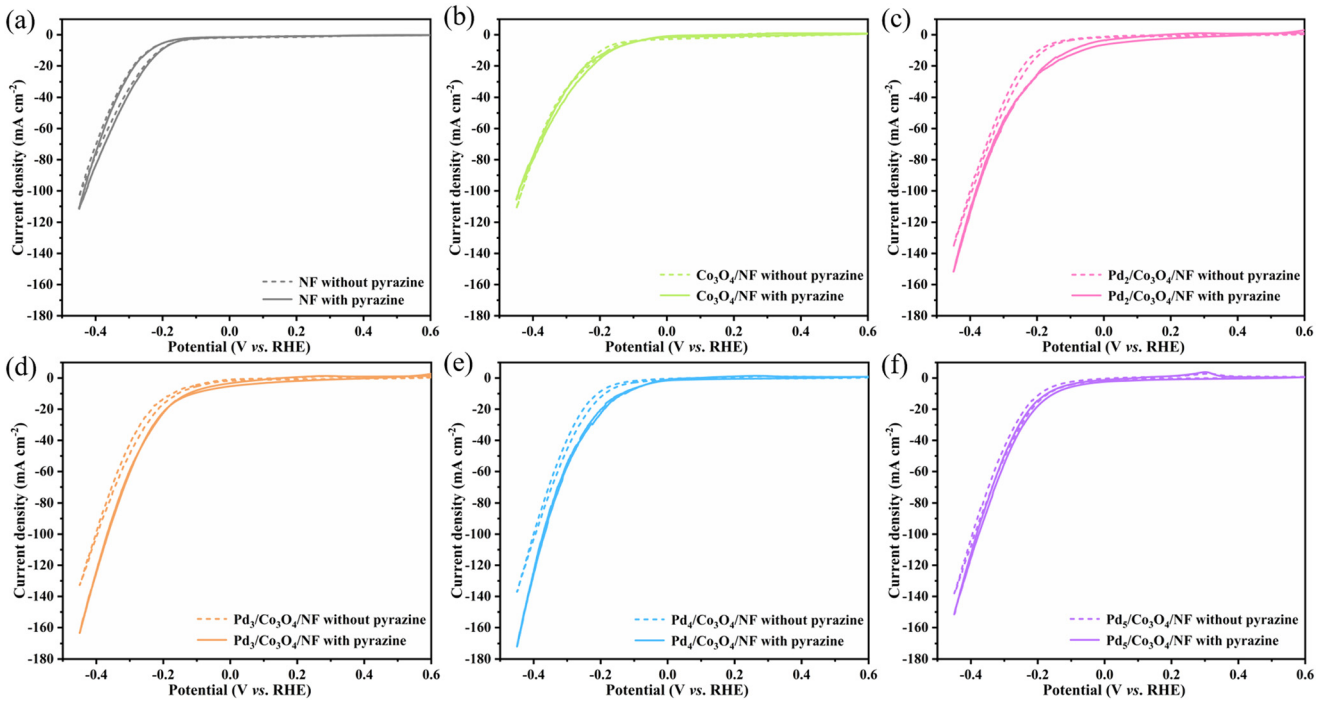

Fig. 3 CV curves within the potential range of 0.7 V to −0.45 V (*vs.* RHE) at 5 mV s^{-1} of (a) NF, (b) Co_3O_4/NF, (c) Pd_2/Co_3O_4/NF, (d) Pd_3/Co_3O_4/NF, (e) Pd_4/Co_3O_4/NF, and (f) Pd_5/Co_3O_4/NF as the working electrodes in (–) working electrode (pyrazine/piperazine)|1 M KOH + 0.01 M pyrazine||1 M KOH|Pt (OH^-/O_2) (+) with SCE as the reference electrode.

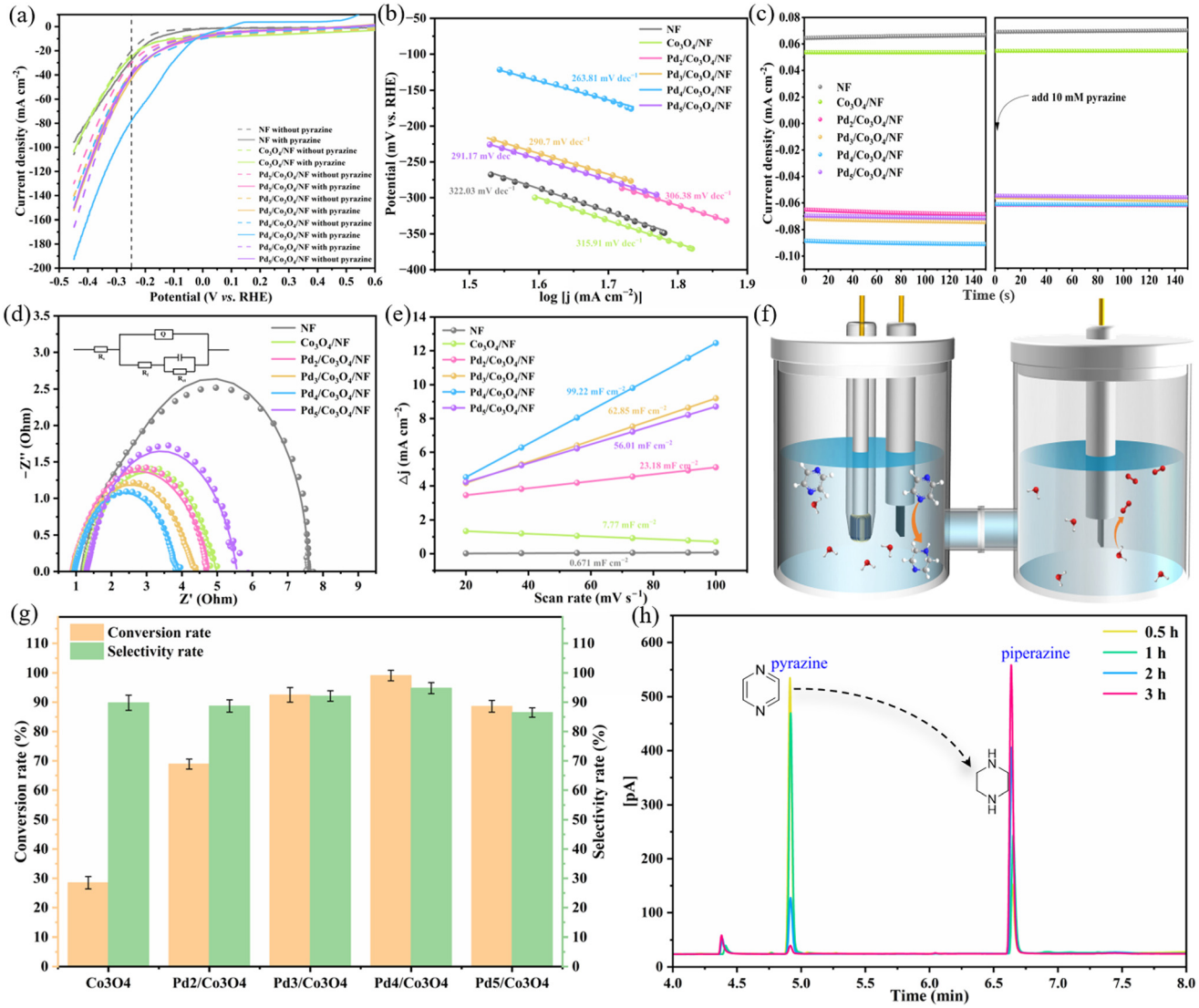

Fig. 4 (a) LSV curves, (b) Tafel plots, (c) OCP profiles, (d) Nyquist plots, (e) C_{dl} values, and (f) schematic diagram of the reaction setup for the catalysts. (g) The conversion and selectivity after chronoamperometry at −0.25 V (*vs.* RHE) for 3 h. (h) The concentration of pyrazine and piperazine after chronoamperometry at −0.25 V (*vs.* RHE) with various times for Pd_4/Co_3O_4/NF. The points are raw data, and the lines are fitted data.

to those of Pd_4/Co_3O_4/NF, both the HER current and the net current of Pd_5/Co_3O_4/NF decreased. This was likely due to excessive Pd loading causing nanoparticle agglomeration, which reduced the number of active sites and intrinsic catalytic activity (Fig. 4a). This observation was consistent with the SEM results.

The commercial Pd/C catalyst exhibited a hydrogen evolution current of −31.0 mA cm^{-2} at −0.25 V (*vs.* RHE). The current remained essentially unchanged after the addition of pyrazine, and a net current only appeared at more negative potentials (Fig. S2a). This is primarily due to the binder used to immobilize Pd/C on the NF surface, which is nearly non-conductive and partially hinders the catalytic performance of Pd/C. Moreover, Pd/C shows relatively poor dispersion, resulting in an electrochemically active surface area much smaller than that of Pd_4/Co_3O_4/NF.

3.2.3 Tafel slope. The Tafel slopes from low to high were Pd_4/Co_3O_4/NF (263.81 mV dec^{-1}), Pd_3/Co_3O_4/NF (290.7 mV dec^{-1}), Pd_5/Co_3O_4/NF (291.17 mV dec^{-1}), Pd_2/Co_3O_4/NF (306.38 mV dec^{-1}), Co_3O_4/NF (315.91 mV dec^{-1}), and NF (322.03 mV dec^{-1}). Pd_4/Co_3O_4/NF demonstrated the smallest Tafel slope (Fig. 4b), which achieved a greater increase in current density per unit overpotential, possessed faster reaction kinetics, and facilitated a more efficient electrode process.

3.2.4 OCP. OCP was a sensitive indicator for changes in pyrazine adsorption within the Helmholtz layer. A stronger interaction between the catalyst surface and pyrazine resulted in a more significant OCP shift upon pyrazine introduction.[40] The OCP of Pd_4/Co_3O_4/NF exhibited the largest negative shift after pyrazine was added (Fig. 4c). This provided direct evidence that its surface had the strongest adsorption affinity for pyrazine molecules. This strong

adsorption stemmed from Pd's inherent high reactivity towards N-heterocyclic compounds and the optimized adsorption strength at Pd sites due to favorable electronic synergy with the Co_3O_4 support. Effective reactant adsorption was a critical prerequisite for achieving highly efficient electrocatalytic hydrogenation.

3.2.5 EIS. All electrocatalysts exhibited similar the solution resistance (R_s) values. The charge transfer resistance (R_{ct}) values at −0.25 V (*vs.* RHE) of NF, Co_3O_4/NF, Pd_2/Co_3O_4/NF, Pd_3/Co_3O_4/NF, Pd_4/Co_3O_4/NF, and Pd_5/Co_3O_4/NF were 6.372, 4.219, 3.846, 3.419, 2.892, and 3.691 ohm, respectively (Fig. 4d and Table S1). Pd_4/Co_3O_4/NF displayed the smallest R_{ct}, indicating the least hindrance to electron transfer at the electrode/electrolyte interface. This facilitated easier interaction with pyrazine and promoted the ECH reaction. The minimal R_{ct} was primarily attributed to the strong electronic interaction between Pd and the Co_3O_4 support. The interfacial electron redistribution, evidenced by the XPS results, not only optimized the electronic structure of the Pd active sites but also induced the formation of more oxygen vacancies in the support. Together, these effects created a highly efficient pathway for interfacial charge transport, significantly accelerating electron transfer during the electrochemical reaction.

3.2.6 C_{dl} and ECSA. The C_{dl} of Pd_4/Co_3O_4/NF, Pd_3/Co_3O_4/NF, Pd_5/Co_3O_4/NF, Pd_2/Co_3O_4/NF, Co_3O_4/NF, and NF were 99.22, 62.85, 56.1, 23.18, 7.77 and 0.671 mF cm^{-2}, respectively (Fig. 4e and S3 and Table S1) and the corresponding ECSAs were 2480.5, 1571.25, 1400.25, 579.5, 194.25 and 16.775 cm^2. Loading Co_3O_4 onto the NF substrate served a dual purpose. It significantly increased the ECSA and promoted stronger integration of Pd with the catalytic support. The C_{dl} and ECSA of Pd_4/Co_3O_4/NF were markedly higher than those of the other catalysts, indicating a greater number of available catalytic active sites. This was primarily attributed to its unique hierarchical nanostructure. The optimal amount of Pd was loaded as highly dispersed nanoparticles onto the nanoneedles (Fig. 2j–l). This configuration maximized the exposure of active sites without compromising the conductive network of the substrate, resulting in a composite structure with a high specific surface area and significant synergistic effects. Furthermore, the abundant oxygen vacancies within the material contributed additional active sites.

3.2.7 Chronoamperometry. The pyrazine hydrogenation of the catalysts in 1 M KOH + 0.01 M pyrazine was conducted with chronoamperometry at −0.25 V (*vs.* RHE) for 3 h (Fig. 4h). After 2 h, the conversion of pyrazine slowed significantly. This was due to the competitive relationship between the electrochemical hydrogenation of pyrazine and the hydrogen evolution reaction (HER). In the later stage of the hydrogenation process, the extremely low substrate concentration allowed the HER to gradually dominate, thereby limiting the further generation of the target product. The differences of pyrazine conversion and piperazine selectivity clearly demonstrated the performance variation among the samples (Fig. 4g and Table S1). Each catalyst was subjected to three independent experiments; the average conversion rates of Co_3O_4/NF, Pd_2/Co_3O_4/NF, Pd_3/Co_3O_4/NF, Pd_4/Co_3O_4/NF, and Pd_5/Co_3O_4/NF were 28.5%, 68.9%, 92.5%, 99.1%, and 88.6% respectively, and the corresponding selectivity rates were 89.8%, 88.7%, 92.1%, 94.8%, and 86.5%. The commercial Pd/C/NF catalyst showed a conversion of 65.2% and a selectivity of 84.4% (Fig. S2b). Pd_4/Co_3O_4/NF exhibited the strongest catalytic capability for converting pyrazine to piperazine. This was because it simultaneously provided an ample supply of H* and demonstrated strong selective adsorption towards pyrazine molecules. The schematic illustration of the pyrazine ECH process in the H-cell is provided in Fig. 4f.

3.2.8 Stability evaluation. The ECH potential of pyrazine for Pd_4/Co_3O_4/NF was optimized. Both the conversion rate and the catalytic current increased with more negative potentials. However, beyond −0.25 V (*vs.* RHE), the conversion rate plateaued while the selectivity reached its maximum of 95.8%. Therefore, −0.25 V (*vs.* RHE) was identified as the optimal potential for pyrazine ECH from an energy-saving perspective (Fig. 5a). The stability of Pd_4/Co_3O_4/NF was assessed through eight chronoamperometry tests at −0.25 V (*vs.* RHE) for 3 h. The highest current density was observed in the first cycle. The current density fluctuated within a reasonable range in subsequent tests, with a noticeable decay appearing only by the 8th cycle. The initial conversion was 98.7%, and all conversions of subsequent cycles were maintained above 98%. The highest value among them was 99.7%. The initial selectivity was 94.7%, and the selectivity remained above 93% for the first 5 cycles, decreased to 86.8% in the sixth cycle, and stabilized to ~87% thereafter (Fig. 5b). However, the faradaic efficiencies over 8 cycles were 33.3%, 31.0%, 29.0%, 30.6%, 31.5%, 28.6%, 30.5% and 31.0%, respectively, which are relatively low. This was primarily because the previous study overemphasized conversion and selectivity, leading to the intentional extension of the reaction time for pyrazine hydrogenation to 3 h. As the reaction progressed, the HER gradually dominated the process, causing the faradaic efficiency to decline over time. These results demonstrated the excellent durability and stability of Pd_4/Co_3O_4/NF. The LSV curve after 8 cycles was nearly identical to that of the initial Pd_4/Co_3O_4/NF (Fig. 5c and d), further confirming its robust stability. A chronoamperometry test for 100 h of Pd_4/Co_3O_4/NF in 1 M KOH + 0.8 M pyrazine was conducted, and the current remained virtually unchanged throughout this extended period, indicating exceptional stability (Fig. 5e). The SEM images of Pd_4/Co_3O_4/NF after chronoamperometry for 8 cycles showed that the nanoneedle substrate structure was largely preserved, although the surface of the needles became rougher. Some detachment of Pd agglomerates was also observed (Fig. S4). Overall, the morphology remained largely intact, confirming good structural stability.

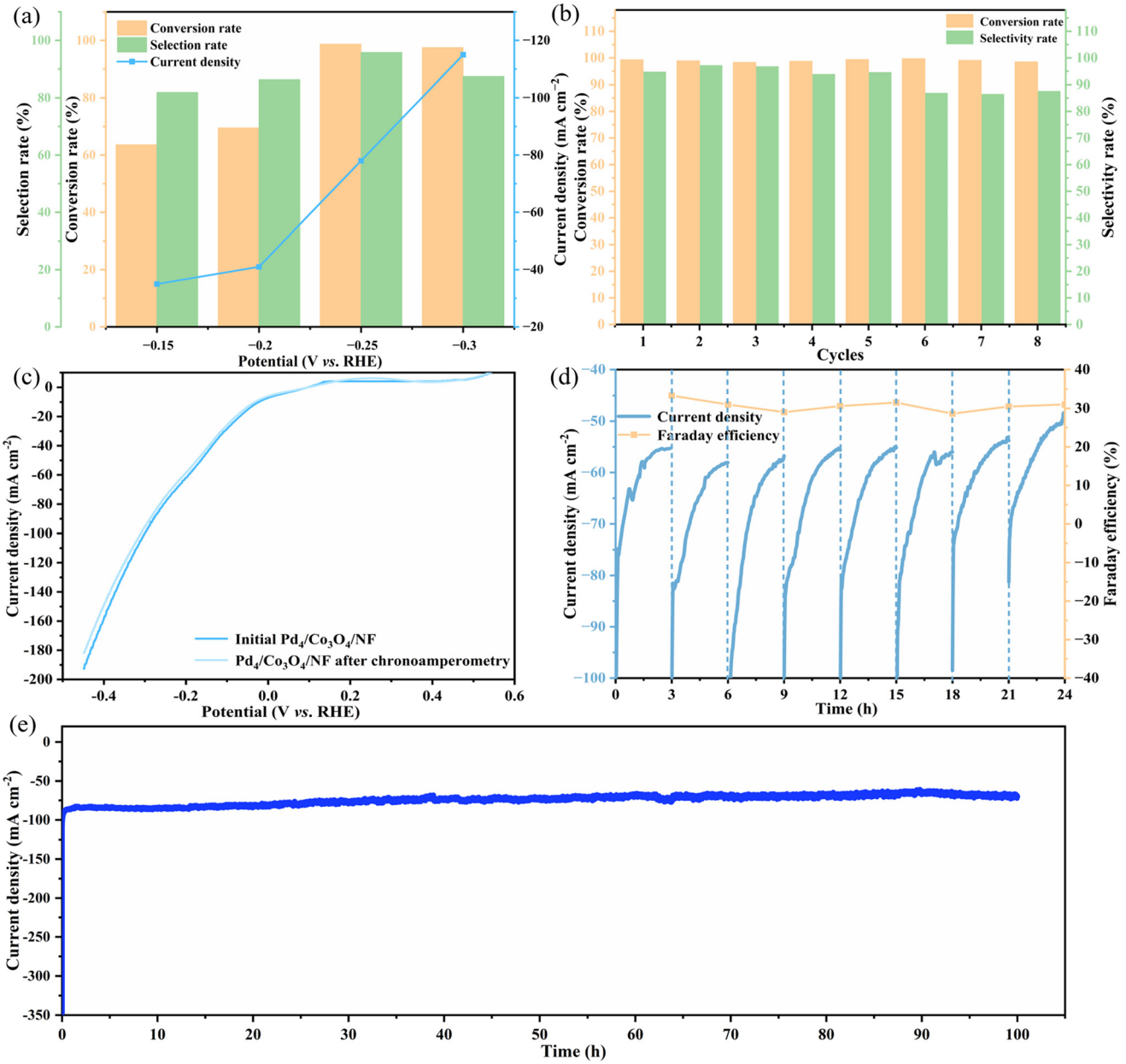

Fig. 5 Electrochemical characteristics of Pd_4/Co_3O_4/NF in the (−) Pd_4/Co_3O_4/NF (pyrazine/piperazine)|1 M KOH + 10 mM pyrazine||1 M KOH|Pt (OH^-/O_2) (+). (a) Pyrazine conversion and piperazine selectivity of chronoamperometry for 3 h at different potentials. (b) Conversion rate and selectivity rate at −0.25 V (*vs.* RHE) with 8 consecutive cycles. (c) LSV curves before and after chronoamperometry for 8 cycles. (d) The chronoamperometry curve at −0.25 V (*vs.* RHE) for 8 cycles with a cycle of 3 h. (e) The chronoamperometry curve at −0.25 V (*vs.* RHE) for 100 h of Pd_4/Co_3O_4/NF with 1 M KOH + 0.8 M pyrazine.

3.3 Pyrazine ECH mechanism of Pd_4/Co_3O_4/NF

3.3.1 pH-dependent experiments. The HER was the primary side reaction competing with pyrazine ECH, and its kinetics were strongly influenced by pH. LSV tests were conducted on Pd_4/Co_3O_4/NF across different pH. The current density gradually increased with higher pH (Fig. 6a). A linear relationship was observed between pH and the logarithm of the current density, yielding a slope of 0.248. A slope greater than zero indicated that the potential-determining step (PDS) of the reaction involves the simultaneous transfer of the proton and the electron, and this confirmed the PCET pathway.[41]

3.3.2 Pyrazine concentration-dependent experiments. The dependence of the ECH rate on the pyrazine concentration of Pd_4/Co_3O_4/NF was analyzed with different concentrations. A decrease in current density was observed as the pyrazine concentration increased from 10 mM to 50 mM (Fig. 6b). The negative reaction order with respect to pyrazine concentration suggested competitive adsorption between H* and pyrazine molecules. The decline in the ECH rate, due to reduced H* coverage, further refined the PCET mechanism for pyrazine hydrogenation to a hydrogen atom transfer (HAT) mechanism. In the HAT mechanism, H* was generated

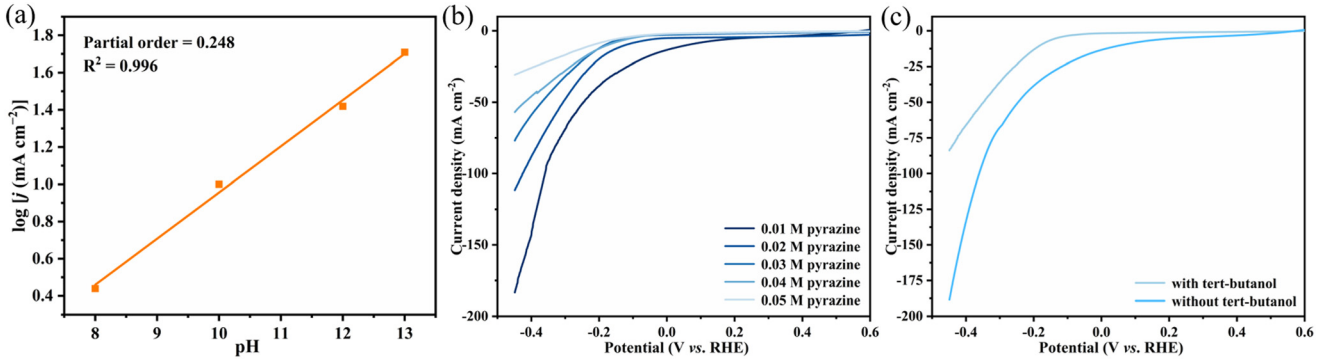

Fig. 6 (a) pH-dependent curve in 1 M KOH + 0.01 M pyrazine, (b) LSV curves with different concentrations of pyrazine, (c) LSV curves of 0.6 to −0.445 V (*vs.* RHE) with and without 0.5 mL *t*-BuOH of Pd_4/Co_3O_4/NF. The points are raw data, and the lines are fitted data.

first and subsequently hydrogenates pyrazine, following the Langmuir–Hinshelwood model.[39,41]

3.3.3 Investigation of H* source. Usually *tert*-butanol (*t*-BuOH) was used as a quencher for H*. The presence of *t*-BuOH significantly suppressed the hydrogenation of pyrazine (Fig. 6c). This demonstrates that the H* species generated during the Volmer step were crucial intermediates controlling the reaction process.[16,17,39] After 8 cycles, the O 1s spectrum of Pd_4/Co_3O_4/NF still showed a predominant O_V signal. However, the O_C content increased significantly, indicating the adsorption of OH^- species from the solution onto the catalyst surface (Fig. 7a). In the Co 2p spectrum (Fig. 7b), the peaks at 779.31 and 794.27 eV were attributed to Co^{3+}, while those at 781.13 and 795.66 eV were assigned to Co^{2+}. These states showed little difference compared to the initial Pd_4/Co_3O_4/NF. The main change was observed in the Pd 3d spectrum (Fig. 7c). The peaks at 335.30 and 339.67 eV correspond to Pd^0 $3d_{5/2}$ and Pd^0 $3d_{3/2}$, respectively, and the peaks for Pd^{2+} $3d_{5/2}$ and Pd^{2+} $3d_{3/2}$ appeared at 337.72 and 342.63 eV. The spectrum indicated that Pd primarily existed as Pd^{2+} after the cycling tests. It was reasonable to speculate that Pd^0 acted as the active site, and these Pd^0 species were oxidized to Pd^{2+} during the pyrazine ECH.

3.3.4 Reaction pathway. In the electrocatalytic hydrogenation of pyrazine over Pd_4/Co_3O_4/NF, the abundant O_Vs on the Co_3O_4 nanostructure surface played a crucial role. Besides enhancing the adsorption of Pd atoms on the Co_3O_4/NF support, these O_Vs also promoted high Pd dispersion and utilization efficiency.[42] Pd acted as a dual-function site for both H* generation and pyrazine adsorption, serving as the primary center for hydrogenating pyrazine to piperazine (Fig. 8). Specifically, Pd catalyzed water molecules *via* the Volmer step to produce H*, which adsorbed on its surface. Simultaneously, a neighboring Pd site adsorbed a pyrazine molecule. The generated H* then spilt over the catalyst surface to the pyrazine-adsorbed site. The adsorbed pyrazine interacted with H* and underwent hydrogenation. The hydrogenation proceeded through consecutive PCET steps, ultimately achieving efficient and highly selective conversion of pyrazine to piperazine. Finally, piperazine desorbed into the solution, re-exposing the Pd active sites for the next cycle of electrocatalytic pyrazine hydrogenation.

4 Conclusion

A series of Pd_x/Co_3O_4/NF (x = 2, 3, 4, 5) as electrocatalysts of pyrazine ECH were successfully synthesized *via* hydrothermal and room-temperature reduction methods. Their ECH mechanism and the performance of pyrazine were systematically investigated. Among them, Pd_4/Co_3O_4/NF demonstrated the optimal electrochemical activity. It achieved a remarkable conversion rate of 99.4% with a

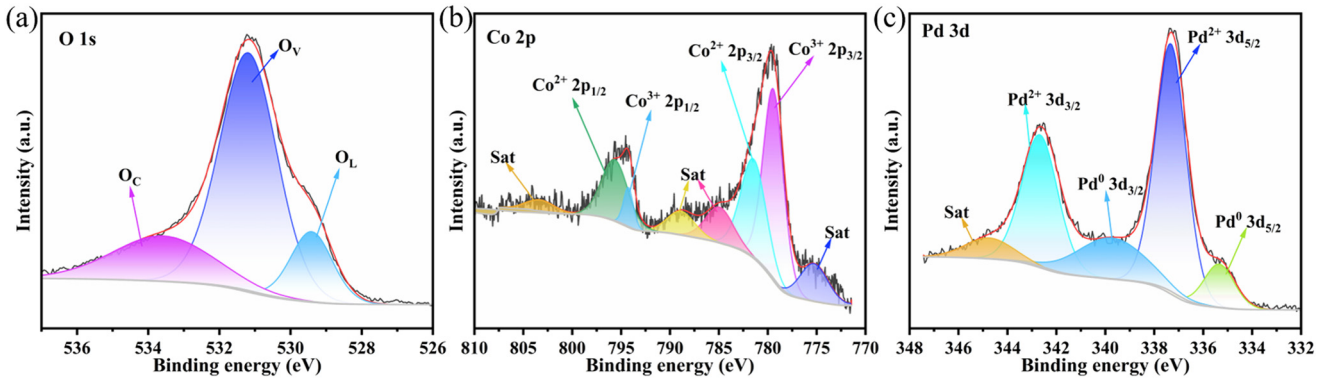

Fig. 7 (a) O 1s, (b) Co 2p, and (c) Pd 3d XPS spectra of Pd_4/Co_3O_4/NF after chronoamperometry of 8 cycles.

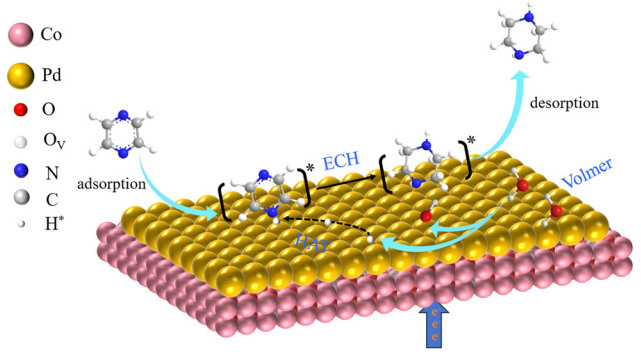

Fig. 8 ECH reaction diagram for the formation of piperazine from pyrazine.

selectivity rate of 97.1% under ambient temperature and pressure. Furthermore, Pd_4/Co_3O_4/NF maintained high electrocatalytic activity and a largely unchanged microstructure after chronoamperometry of 8 cycles, highlighting its excellent stability. Mechanistic studies revealed that Pd acted as the catalytic center with dual functions, which promoted water electrolysis to generate H* and also facilitated the adsorption of pyrazine, providing the active sites for ECH. The direct growth of the Co_3O_4 layer on the NF substrate offered abundant anchoring sites for Pd, resulting in a tight interfacial structure. The Co atoms modulated the electronic structure and through strong metal–support interactions enhanced the adsorption–desorption behavior of H* and organic molecules on Pd. Compared to traditional hydrogen storage systems, pyrazine ECH with Pd_4/Co_3O_4/NF was safer, more environmentally friendly, and simpler. It will eliminate the need for harsh reaction conditions and is compatible with green electricity generated from wind, water, and other renewable sources, demonstrating broad application prospects and providing an important reference for future research.

Nonetheless, this study also acknowledges a limitation, that is, the obtained faradaic efficiency remains relatively low. This aspect leaves considerable room for improvement in future work. Further optimization of catalyst design and reaction conditions should focus on enhancing charge utilization efficiency while maintaining high conversion and selectivity, which is crucial for the practical deployment of electrocatalytic LOHC systems.

Conflicts of interest

There are no conflicts to declare.

Data availability

All study data are included in the article and/or supplementary information (SI) Appendix.

Supplementary information: electrochemical tests and corresponding parameters, and SEM images, EDS mapping of the catalysts. See DOI: https://doi.org/10.1039/d5lf00408j.

Acknowledgements

This work was supported by the R&D Project of China Southern Power Grid Co., Ltd (YNKJXM20240023).

References

1 M. Barani, K. Löffler, P. C. del Granado, N. Moskalenko, E. Panos, F. M. Hoffart, C. von Hirschhausen, M. Kannavou, H. Auer, K. Hainsch, T. G. Grandón, S. Mathisen and A. Tomasgard, European energy vision 2050 and beyond: Designing scenarios for Europe's energy transition, *Renewable Sustainable Energy Rev.*, 2026, **225**, 116074, DOI: 10.1016/j.rser.2025.116074.

2 Z. Wang, X. Liu, W. Gu, L. Cheng, H. Wang, J. Liu, L. Li, J. Wang, M. Zhang, Y. Wang and Y. Shen, Power-to-hydrogen-to-power as a pathway for wind and solar renewable energy utilization in China: Opportunities and challenges, *Renewable Sustainable Energy Rev.*, 2026, **226**, 116195, DOI: 10.1016/j.rser.2025.116195.

3 M. Habibi, M. G. Hosseini and K. Wang, Toward sustainable energy: A comprehensive review of hydrogen production, storage, and utilization, *Renewable Sustainable Energy Rev.*, 2026, **226**, 116193, DOI: 10.1016/j.rser.2025.116193.

4 Z. Hua, W. Gao, S. Chi, X. Wang and J. Zheng, Development status and challenges of high-pressure gaseous hydrogen storage vessels and cylinders in China, *Renewable Sustainable Energy Rev.*, 2025, **214**, 115567, DOI: 10.1016/j.rser.2025.115567.

5 X. Xu, H. Xu, J. Zheng, L. Chen and J. Wang, A high-efficiency liquid hydrogen storage system cooled by a fuel-cell-driven refrigerator for hydrogen combustion heat recovery, *Energy Convers. Manage.*, 2020, **226**, 113496, DOI: 10.1016/j.enconman.2020.113496.

6 J. K. Abifarin, J. F. Torres and Y. Lu, 2D materials for enabling hydrogen as an energy vector, *Nano Energy*, 2024, **129**, 109997, DOI: 10.1016/j.nanoen.2024.109997.

7 Y. Li, X. Guo, S. Zhang and Y. He, A perspective review on N-heterocycles as liquid organic hydrogen carriers and their hydrogenation/dehydrogenation catalysts, *Energy Fuels*, 2024, **38**, 12447–12471, DOI: 10.1021/acs.energyfuels.4c01633.

8 K. C. Tan, T. He, Y. S. Chua and P. Chen, Recent advances of catalysis in the hydrogenation and dehydrogenation of N-heterocycles for hydrogen storage, *J. Phys. Chem. C*, 2021, **125**, 18553–18566, DOI: 10.1021/acs.jpcc.1c04783.

9 L. Liu, Q. Zhang, C. Deng, C. Li, Y. Zhao, R. Gao, T. Zhu, Y. Dong, H. Cheng and M. Yang, Pyridine N-induced intra-pore and interfacial dual-confined Pd^0-$Pd^{\delta+}$ synergistic catalysis for ultra-stable dehydrogenation of dodecahydro-N-propylcarbazole, *Appl. Catal., B*, 2024, **351**, 123987, DOI: 10.1016/j.apcatb.2024.123987.

10 M. Yang, G. Cheng, D. Xie, T. Zhu, Y. Dong, H. Ke and H. Cheng, Study of hydrogenation and dehydrogenation of 1-methylindole for reversible onboard hydrogen storage application, *Int. J. Hydrogen Energy*, 2018, **43**, 8868–8876, DOI: 10.1016/j.ijhydene.2018.03.134.

11 Y. Dong, H. Zhao, Y. Zhao, M. Yang, H. Zhang and H. Cheng, Study of catalytic hydrogenation and dehydrogenation of 2,3-dimethylindole for hydrogen storage application, *RSC Adv.*, 2021, **11**, 15729–15737, DOI: 10.1039/d1ra01552d.

12 Y. Dong, M. Yang, Z. Yang, H. Ke and H. Cheng, Catalytic hydrogenation and dehydrogenation of N-ethylindole as a new heteroaromatic liquid organic hydrogen carrier, *Int. J. Hydrogen Energy*, 2015, **40**, 10918–10922, DOI: 10.1016/j.ijhydene.2015.05.196.

13 Z. Chen, M. Yang, T. Zhu, Z. Zhang, X. Chen, Z. Liu, Y. Dong, G. Cheng and H. Cheng, 7-ethylindole: A new efficient liquid organic hydrogen carrier with fast kinetics, *Int. J. Hydrogen Energy*, 2018, **43**, 12688–12696, DOI: 10.1016/j.ijhydene.2018.03.088.

14 O. Lebedeva, D. Kultin, A. Kalenchuk and L. Kustov, Advances and prospects in electrocatalytic hydrogenation of aromatic hydrocarbons for synthesis of "loaded" liquid organic hydrogen carriers, *Curr. Opin. Electrochem.*, 2023, **38**, 101207, DOI: 10.1016/j.coelec.2022.101207.

15 Y. Pan, Z. Bao, C. Wang, Z. Wang, P. Xu, X. Bai, X. Shi, H. Zheng, H.-E. Wang and L. Zheng, Electrochemical hydrogenation of quinoline enabled by Cu^0-Cu^+ dual sites coupled with efficient biomass valorization in aqueous solution, *Adv. Funct. Mater.*, 2024, **35**, 2414120, DOI: 10.1002/adfm.202414120.

16 S. Guo, Y. Wu, C. Wang, Y. Gao, M. Li, B. Zhang and C. Liu, Electrocatalytic hydrogenation of quinolines with water over a fluorine-modified cobalt catalyst, *Nat. Commun.*, 2022, **13**, 5297, DOI: 10.1038/s41467-022-32933-6.

17 M. Li, C. Liu, Y. Huang, S. Han and B. Zhang, Water-involving transfer hydrogenation and dehydrogenation of N-heterocycles over a bifunctional $MoNi_4$ electrode, *Chin. J. Catal.*, 2021, **42**, 1983–1991, DOI: 10.1016/S1872-2067(21)63834-2.

18 N. Shida, Y. Shimizu, A. Yonezawa, J. Harada, Y. Furutani, Y. Muto, R. Kurihara, J. N. Kondo, E. Sato, K. Mitsudo, S. Suga, S. Iguchi, K. Kamiya and M. Atobe, Electrocatalytic hydrogenation of pyridines and other nitrogen-containing aromatic compounds, *J. Am. Chem. Soc.*, 2024, **146**, 30212–30221, DOI: 10.1021/jacs.4c09107.

19 Y. Inami, H. Ogihara, S. Nagamatsu, K. Asakura and I. Yamanaka, Synergy of Ru and Ir in the electrohydrogenation of toluene to methylcyclohexane on a Ketjenblack-supported Ru-Ir alloy cathode, *ACS Catal.*, 2019, **9**, 2448–2457, DOI: 10.1021/acscatal.8b03610.

20 G. Yang, V. Maliekkal, X. Chen, S. Eckstein, H. Shi, D. M. Camaioni, E. Baráth, G. L. Haller, Y. Liu, M. Neurock and J. A. Lercher, Rate enhancement of phenol hydrogenation on Pt by hydronium ions in the aqueous phase, *J. Catal.*, 2021, **404**, 579–593, DOI: 10.1016/j.jcat.2021.11.003.

21 S. Sarkar and S. C. Peter, An overview on Pd-based electrocatalysts for the hydrogen evolution reaction, *Inorg. Chem. Front.*, 2018, **5**, 2060–2080, DOI: 10.1039/c8qi00042e.

22 L. C. Meyer, U. Sanyal, K. A. Stoerzinger, K. Koh, J. L. Fulton, D. M. Camaioni, O. Y. Gutiérrez and J. A. Lercher, Influence of the molecular structure on the electrocatalytic hydrogenation of carbonyl groups and H_2 evolution on Pd, *ACS Catal.*, 2022, **12**, 11910–11917, DOI: 10.1021/acscatal.2c03207.

23 H. Sun, Z. Yan, F. Liu, W. Xu, F. Cheng and J. Chen, Self-supported transition-metal-based electrocatalysts for hydrogen and oxygen evolution, *Adv. Mater.*, 2020, **32**, 1806326, DOI: 10.1002/adma.201806326.

24 Z. Yan, H. Sun, X. Chen, H. Liu, Y. Zhao, H. Li, W. Xie, F. Cheng and J. Chen, Anion insertion enhanced electrodeposition of robust metal hydroxide/oxide electrodes for oxygen evolution, *Nat. Commun.*, 2018, **9**, 2373, DOI: 10.1038/s41467-018-04788-3.

25 H. Yuan, S. Wang, Z. Ma, M. Kundu, B. Tang, J. Li and X. Wang, Oxygen vacancies engineered self-supported B doped Co_3O_4 nanowires as an efficient multifunctional catalyst for electrochemical water splitting and hydrolysis of sodium borohydride, *Chem. Eng. J.*, 2021, **404**, 126474, DOI: 10.1016/j.cej.2020.126474.

26 Y. Jiang, H. Liu, Y. Jiang, Y. Mao, W. Shen, M. Li and R. He, Adjustable heterointerface-vacancy enhancement effect in RuO_2@Co_3O_4 electrocatalysts for efficient overall water splitting, *Appl. Catal., B*, 2023, **324**, 122294, DOI: 10.1016/j.apcatb.2022.122294.

27 Q. Liao, M. Shi, Q. Zhang, W. Cheng, P. Ji, X. Fu, H. Lai, R. Fan, J. Sheng and H. Li, Gold catalyst anchored to pre-reduced Co_3O_4 nanorods for the hydrodeoxygenation of vanillin using alcohols as hydrogen donors, *ACS Appl. Mater. Interfaces*, 2022, **14**, 3939–3948, DOI: 10.1021/acsami.1c18197.

28 Z. Bai, L. Li, P. Yin and T. Lei, Ultralow iridium content and oxygen vacancy-rich Ir–Co_3O_4 electrocatalyst to boost acidic oxygen evolution, *Int. J. Hydrogen Energy*, 2025, **128**, 76–84, DOI: 10.1016/j.ijhydene.2025.04.230.

29 C. C. L. McCrory, S. Jung, J. C. Peters and T. F. Jaramillo, Benchmarking heterogeneous electrocatalysts for the oxygen evolution reaction, *J. Am. Chem. Soc.*, 2013, **135**, 16977–16987, DOI: 10.1021/ja407115p.

30 C. Feng, L. Xuebin, C. Wei, W. Na and J. Yanqiao, Double core-shell hollow nanocage CuO@Co_3O_4 for the selective hydrogenolysis of C–O bonds of lignin without external hydrogen, *Chem. Eng. J.*, 2024, **491**, 152002, DOI: 10.1016/j.cej.2024.152002.

31 S. Wang, S. Zhang, Z. Zhang, Y. Tan, K. Liang, X. Guo and X. Kong, Reversible electrochemical hydrogen storage of quinoxaline utilizing Pd/NF dual-function electrocatalyst under mild conditions, *Int. J. Hydrogen Energy*, 2024, **49**, 719–728, DOI: 10.1016/j.ijhydene.2023.07.089.

32 T. A. Revathy, K. Dhanapal, S. Dhanavel, V. Narayanan and A. Stephen, Pulsed electrodeposited dendritic Pd-Ni alloy as a magnetically recoverable nanocatalyst for the hydrogenation of 4-nitrophenol, *J. Alloys Compd.*, 2018, **735**, 1703–1711, DOI: 10.1016/j.jallcom.2017.11.264.

33 T. Wang, P. Wang, W. Zang, X. Li, D. Chen, Z. Kou, S. Mu and J. Wang, Nanoframes of Co_3O_4-Mo_2N heterointerfaces enable high-performance bifunctionality toward both

electrocatalytic HER and OER, *Adv. Funct. Mater.*, 2022, **32**, 2107382, DOI: 10.1002/adfm.202107382.

34 Z. Feng and X. Bai, Enhanced activity of bimetallic Pd-Ni nanoparticles on KIT-6 for production of hydrogen from dodecahydro-N-ethylcarbazole, *Fuel*, 2022, **329**, 125473, DOI: 10.1016/j.fuel.2022.125473.

35 Z. Zhang, Z. Yang, C. Wei, Z. Liu and T. Mu, Facet-dependent electrocatalytic oxidation activity of Co_3O_4 nanocrystals for 5-hydroxymethylfurfural, *Green Chem.*, 2023, **25**, 8196–8206, DOI: 10.1039/d3gc02398b.

36 M. Lan, B. Liu, R. Zhao, M. Dong, X. Wang, L. Fang and L. Wang, Dandelion-like $CuCo_2O_4$ arrays on Ni foam as advanced positive electrode material for high-performance hybrid supercapacitors, *J. Colloid Interface Sci.*, 2020, **566**, 79–89, DOI: 10.1016/j.jcis.2020.01.077.

37 M. Zeng and Y. Li, Recent advances in heterogeneous electrocatalysts for the hydrogen evolution reaction, *J. Mater. Chem. A*, 2015, **3**, 14942–14962, DOI: 10.1039/c5ta02974k.

38 W. Zhao, W. Fu, H. Yang, C. Tian, M. Li, Y. Li, L. Zhang, Y. Sui, X. Zhou, H. Chen and G. Zou, Electrodeposition of Cu2O films and their photoelectrochemical properties, *CrystEngComm*, 2011, **13**, 2871–2877, DOI: 10.1039/c0ce00829j.

39 Z.-C. Yao, J. Chai, T. Tang, L. Ding, Z. Jiang, J. Fu, X. Chang, B. Xu, L. Zhang, J.-S. Hu and L.-J. Wan, Manipulating hydrogenation pathways enables economically viable electrocatalytic aldehyde-to-alcohol valorization, *Proc. Natl. Acad. Sci. U. S. A.*, 2025, **122**, e2423542122, DOI: 10.1073/pnas.2423542122.

40 T. Cao, J. Cheng, Y. Xiang, L. Hu, X. Hu, L. Li, X. Huang and Z. Wei, Activating surface oxygen in Ce/Mo-Doped Ni oxyhydroxide for synergistically enhancing furfural oxidation and hydrogen evolution at ampere-level current densities, *Angew. Chem., Int. Ed.*, 2025, **64**, e202506017, DOI: 10.1002/anie.202506017.

41 C. Chauhan, T. Gupta and B. Mondal, Deciphering the role of second metal in M-Ni (M = Fe, Ni, and Mn) heterobimetallic electrocatalysts in controlling the HAT versus hydride transfer mechanism for the dehydrogenation of alcohols, *Small*, 2025, **21**, 2410228, DOI: 10.1002/smll.202410228.

42 Z. Du, W. Ran, H. Zhao, J. Ma, J. Sun, B. Liu, S. Lin and R. Liu, Fully exposed Pd ensembles on ultrathin Co_3O_4 nanosheets: A reductive-oxidative dual-active catalyst for the detoxification of chlorophenol, *ACS ES T Eng.*, 2024, **4**, 1401–1411, DOI: 10.1021/acsestengg.4c00003.